Bioinspired multiscale Al_2O_3-rGO/Al laminated composites with superior mechanical properties

Zhiming Zhang [a], Genlian Fan [a,**], Zhanqiu Tan [a], Haitao Zhao [b], Yanjin Xu [c], Dingbang Xiong [a], Zhiqiang Li [a,*]

[a] *State Key Laboratory of Metal Matrix Composites, School of Materials Science and Engineering, Shanghai Jiao Tong University, Shanghai, 200240, China*
[b] *School of Aeronautics and Astronautics, Shanghai Jiao Tong University, Shanghai, 200240, China*
[c] *AVIC Manufacturing Technology Institute, Beijing, 100024, China*

ARTICLE INFO

ABSTRACT

Nacre's multiscale reinforcing mechanisms provide lessons for the design and fabrication of high-performance engineering composites. In this study, the addition of hierarchically aligned flake Al_2O_3 and reduced Graphene Oxide (rGO) nanosheets into Al matrix constitute the bioinspired multiscale Al_2O_3-rGO/Al laminated composite via flake powder metallurgy. The results show that multiscale Al_2O_3-rGO reinforcements have the synergistic strengthening effect of $1 + 1 > 2$. Extra strengthening mechanism is attributed to enhanced load transfer due to good bonding at Al_2O_3/rGO/Al interface. Compared to Al_2O_3/Al composite, the uniform elongation of Al_2O_3-rGO/Al laminated composite doesn't decrease due to the higher strain hardening capacity. The work presented here provides a new strategy for developing advanced composites with simultaneous enhancement of the modulus-strength-ductility.

1. Introduction

Taking lessons from nacres' hierarchical architecture to overcome the conflict between strength and toughness of composites has motivated extensive bioinspired research [1]. The key to success of these nacre-inspired materials is to clone the brick-and-mortar structure in nacre, which is composed of 95 wt% aragonite ($CaCO_3$) and 5 wt% organic materials [2,3]. Within the nacre's hierarchical structure, multiple multiscale reinforcing principles are applied to achieve such exceptional mechanical properties [2,4]. At the microscale level, the brick-and-mortar structure is formed by alternately stacking the compound mortar with the aragonite bricks, which act as in-plane load carriers. At the nanoscale level, nanofillers in soft mortar and the nanoasperities/nanobridges at brick/mortar interface are critical factors to dramatic improvement in performance [5–7]. In artificial engineering composites, the addition of multiscale hybrid reinforcements into a soft matrix is a way to reproduce the nacre's hierarchical architecture. These reported researches mainly focus on the polymer [7], epoxy [5], and ceramic [8,9] matrix composites, and only limited studies are for multiscale reinforced metal matrix composites. The following problems are

hindering the development of nacre-like metal matrix composites: 1) How to uniformly disperse the nanofiller in the matrix? Simultaneously adding micro- and nano-reinforcements into metal matrix is still challenging because nanofillers tend to agglomerate at the surface of micro-reinforcements. 2) How to obtain multiscale building blocks, which are alternately stacked to fabricate hierarchical brick-and-mortar structure?

The pre-dispersion on the surface of micro-reinforcement has been used to solve the problem of agglomeration of nanofillers. Li et al. [10, 11] firstly in-situ synthesized carbon nanotube (CNT) on the surface of micro-sized SiC_p to form the SiC_p(CNT) hybrid reinforcement by chemical vapor deposition. It is shown that the hybrid reinforcement strengthened the Al matrix close to particle/matrix interface, and provided effective load transfer ability [12]. However, the lower specific surface area of micro-particle limits the volume fraction of nanofiller in the composite. Zhou et al. [13] found that the ball-milled route could further improve the dispersion efficiency of CNTs in the Mg matrix after the pre-dispersion of CNTs on the surface of SiC, and good combination of ultra-high strength and good ductility was successfully achieved. Therefore, the pre-dispersion of nanofiller is necessary to fabricate the

---

multiscale reinforced composites.

Two-dimensional (2D) reinforcements, such as graphene nanosheets, reduced graphene oxide (rGO) and submicrometer Al_2O_3 platelets, are recently used to fabricate the bioinspired composites. Graphene, as a single-atomic 2D nanomaterial, is an ideal candidate for fabricating graphene-based artificial nacre [14] and graphene/metal nacre-inspired composites [15,16]. In metal matrix composites, adding a low content of graphene into metal exhibits a high reinforcing efficiency. Simultaneous improvements on strength and toughness were achieved in rGO/Cu [16] and rGO/Al [15] nanolaminated composites. Similarly, submicrometer Al_2O_3 platelets have been used as a building block to design the nacre-like materials, which replicated the aragonite brick structure in nacre and yield excellent mechanical performance [17,18]. Although the previous studies have used an individual nano-or micro-reinforcement as a building block, simultaneously adding the multiscale building blocks with graphene and Al_2O_3 remains a challenge.

In the study, flake powder metallurgy (Flake PM), a bottom-up assembly process of composite flake powders, is used to prepare bioinspired multiscale laminated composite. The flake Al_2O_3 and rGO at different scale are combined to fabricate the Al_2O_3-rGO/Al laminated composite with brick-and-mortar structure. The multiscale Al_2O_3-rGO reinforcements have the synergistic strengthening effect of $1 + 1 > 2$. The bioinspired multiscale laminated structure can contribute to simultaneous enhancement of the modulus-strength-ductility that cannot be obtained using individual reinforcement.

2. Experimental methods

2.1. Composite fabrication

The flake Al powders was obtained by ball milling the spherical Al powders with average diameter of 6.5 μm at 135 rpm for 4 h, similar to our previous report [19]. Graphene oxide (GO, 99% purity) powders were provided by Nanjing XFNano Material Tech Co. Ltd., China. Flake Al_2O_3 powders with diameter of ~7.5 ± 2.5 μm and thickness of ~350 ± 150 nm, were acquired from Merck KGaA (Darmstadt, Germany). The processing routes of bioinspired multiscale Al_2O_3-rGO/Al laminated composites via flake PM are illustrated in Fig. 1.

2.1.1. The fabrication of flake GO/Al powders

The flake GO/Al powders are fabricated by a slurry dispersion process based on the electrostatic adsorption mechanism [20,21]. 200 mg GO was added to 200 ml deionized water and then sonicated for 2 h using an ultrasonic homogenizer. The flake Al powders (20 g) were first poured into the anhydrous ethanol (300 ml), and then GO aqueous suspension (28 ml) were mixed and stirred for 3 h on a magnetic stirring apparatus. The flake GO/Al powders were dried at 120 °C under vacuum pressure of 10^{-3} Pa.

2.1.2. Powder mixing

The flake GO/Al powders and 5 vol% Al_2O_3 powders were blended in a jar mill for 12 h using agate balls as grinding media. In the composite, the volume fraction of GO and Al_2O_3 are respectively 0.15%, 5%.

2.1.3. Consolidation

The composite powders were cold-pressed at the pressure of 300 MPa in a φ40 mm die mold, and then pressureless sintered at 540 °C for 2 h under vacuum pressure of 10^{-3} Pa. Subsequently, the billets were hot extruded into φ12.5 mm rods at 693 K with an extrusion ratio of ~10:1 at a ram speed of 12 mm/min. The density of extrude rods were over 99.5%.

For comparison, Al matrix, 0.15 vol% rGO/Al and 5 vol% Al_2O_3/Al composites were fabricated by the same Flake PM process.

2.2. Mechanical and microstructural characterization

Tensile specimens with a cross-section of 2×4 mm^2 and a gauge length of 12 mm were machined along the extrusion direction. Three tensile tests for each set of samples were carried out on a Zwick Z100 testing machine with a mechanical contact extensometer at a constant strain rate of 5×10^{-4} s^{-1} at room temperature. Young's modulus of the sample was measured through resonance test on ET-RT modulus tester (from Nihon-tech, Japan) at room temperature. Three plate-shaped samples with a cross-section of 10×60 mm^2 and a thickness of 2 mm were tested to obtain the average Young's modulus value.

For metallographic analysis, the specimen surface was prepared using conventional metallographic techniques and then went through ion polishing (model of ion polisher: Gatan Ilon). The Raman spectrum (RM, Senterra R200-L) was collected using the 532 nm line of an Ar + laser as the excitation source to validate the structural integrity of graphene. The morphology of powders and composites were characterized using a field emission scanning electron microscope (FE-SEM, TESCAN, RISE) and a high-resolution transmission electron microscopy (HR-TEM, Talos F200X G2). EBSD characterization was performed in MIRA3 SEM equipped with an Oxford Instruments NordlysMax3 electron backscatter diffraction (EBSD) detector with acceleration voltage of 20 kV.

3. Results

3.1. Microstructure characterization of powders and composites

Fig. 2 shows the SEM images and the distribution of GO on the surface of GO/Al powders. The spherical Al powders were flattened into 2D planar morphology during ball milling, and average diameter and thickness of flake Al powders are ~21 ± 5 μm, 400 ± 100 nm respectively. A larger specific surface area of flake Al powders allowed GO to be uniformly absorbed on its surface. GO nanosheets, referred to the dark parts in Fig. 2(b), are uniformly distributed on the surface of flake GO/Al powders, and average lateral dimension of GO nanosheets are estimated to be about 210 nm (Fig. 2(c)).

The Raman spectroscopy of GO, GO/Al powders and the bulk composites are shown in Fig. 3. Generally, *D*-peak intensity is an indication of the degree of disorder which decreases after reduction of GO, and the ratio of *D*-peak to *G*-peak (I_D/I_G ratio) is used to assess the structural damage of graphene [22]. The value of I_D/I_G increases from 0.83 to 0.85 in GO/Al powder, and it suggests that the GO could be slightly damaged after electrostatic adsorption. In the bulk composite, both the decrease
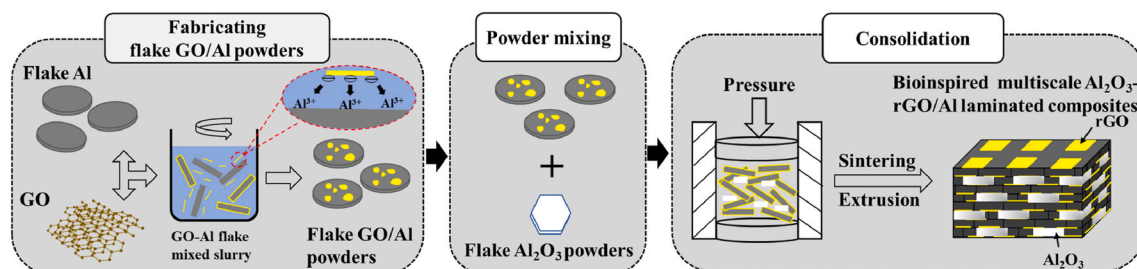

Fig. 1. Schematic diagram of processing routes of bioinspired multiscale Al_2O_3-rGO/Al laminated composites via Flake PM.
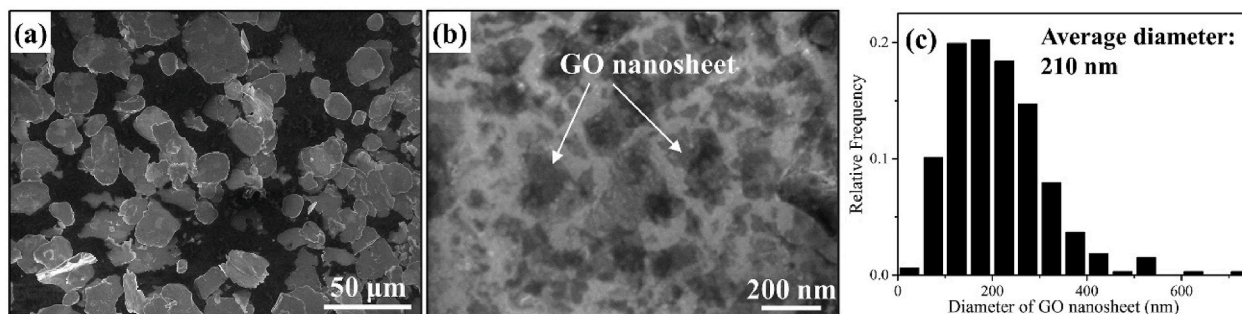
Fig. 2. SEM images of (a, b) GO/Al powders, (c) lateral dimension distribution of GO nanosheet on the surface of Al flake.
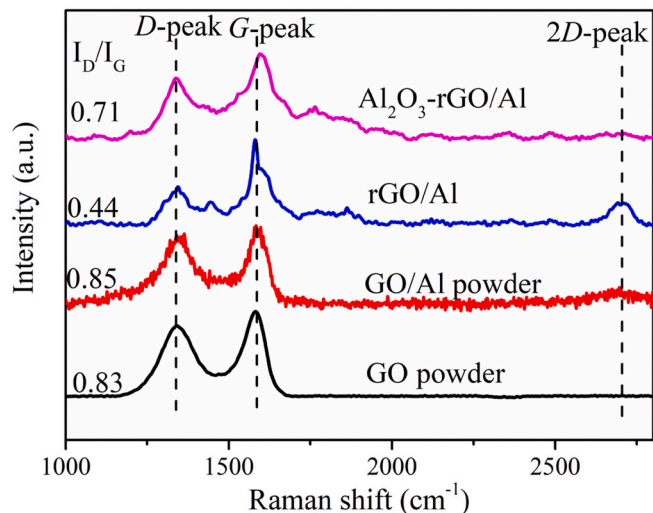

Fig. 3. Raman spectroscopy of GO powder, GO/Al powder and the bulk composites.

of I_D/I_G and the occurrence of well-defined 2D-peak indicates thermal reduction of the original GO to rGO during consolidation, similar to others' works [23,24]. In Al$_2$O$_3$-rGO/Al composite, the I_D/I_G value increases and the G-peak is shifted to a higher wavenumber. The damage of rGO could be caused due to the collision between powders and agate balls during powder mixing.

Fig. 4 shows the SEM images of Al$_2$O$_3$/Al and Al$_2$O$_3$-rGO/Al composites. Flake Al$_2$O$_3$ are parallel-aligned along extrusion direction (ED) and uniformly distributed in Al matrix, forming brick-and-mortar structure. The introduction of rGO into Al$_2$O$_3$/Al composite has no apparent effect on the distribution of Al$_2$O$_3$. The samples exhibit densified microstructure without observable micropores or macroscopic defects.
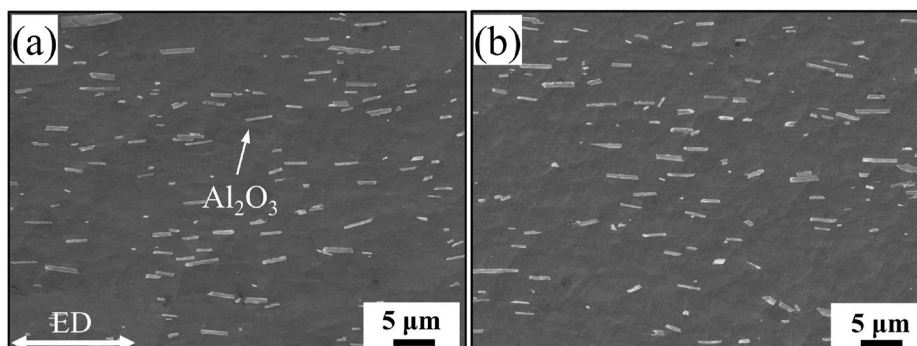
Fig. 5 shows the Bright-field STEM (BF-STEM), Dark-field STEM (DF-STEM) and HRTEM images of Al matrix and Al$_2$O$_3$/Al composites. From O (oxygen) element mapping in Fig. 5(b), there are nano-scaled Al$_2$O$_3$ (n-Al$_2$O$_3$) in Al matrix in addition to the extra flake Al$_2$O$_3$. Both intergranular n-Al$_2$O$_3$ (indicated by white arrows) and intragranular n-Al$_2$O$_3$ (indicated by red arrows) are distributed in the Al matrix, shown in Fig. 5(d, e). According to the element mapping in Fig. 5(i), the intragranular n-Al$_2$O$_3$ is clearly observed in Al [011] grain. It is also observed that there is a n-Al$_2$O$_3$ layer at Al$_2$O$_3$/Al interface. The n-Al$_2$O$_3$ is originated from the native amorphous Al$_2$O$_3$ layer with the thickness of ~5 nm on the surface of flake Al powder, similar to the previous study [19]. As shown in Fig. 5(f), the n-Al$_2$O$_3$ layers at grain boundaries were bent and then broken during the extrusion process and many of them were left inside the recrystallized Al grains due to dynamic recrystallization (DRX), resulting in the formation of intragranular n-Al$_2$O$_3$ with the length of about 200 nm.

Fig. 6 shows the STEM and HRTEM images of rGO/Al and Al$_2$O$_3$-rGO/Al laminated composites. It is observed that flake Al$_2$O$_3$ is surrounded by nanolaminated Al grains in Al$_2$O$_3$-rGO/Al laminated composite. It is observed in Fig. 6(c) that the (002) plane of rGO with interplanar spacing of ~0.34 nm is parallel to the (222) plane of Al$_2$O$_3$. The nano-asperity is formed at Al$_2$O$_3$-rGO-Al interface due to the difference of thickness of adjacent rGO nanosheets. Compared to Al matrix or Al$_2$O$_3$/Al composite (Fig. 5), the n-Al$_2$O$_3$ in rGO/Al or Al$_2$O$_3$-rGO/Al laminated composites is mainly distributed along GBs while only few intragranular n-Al$_2$O$_3$ are observed. Fig. 6(f) shows the HRTEM characterization at Al/rGO/Al interface, showing that the rGO layers (about 3–6 nm) are sandwiched between n-Al$_2$O$_3$ layers. It indicates that the introduction of rGO at GBs can inhibit the broken of n-Al$_2$O$_3$ nanolayers and the DRX is further suppressed during extrusion process. Therefore, the addition of hierarchically aligned Al$_2$O$_3$ and rGO into the Al matrix constitute the nacre-inspired multiscale Al$_2$O$_3$-rGO/Al laminated composite with brick-and-mortar structure.

Fig. 7 show the EBSD images of Al matrix and rGO/Al composite. The rGO/Al composite exhibits obvious laminated structure, but there are some equiaxed or recrystallized grain in Al matrix. The distribution of
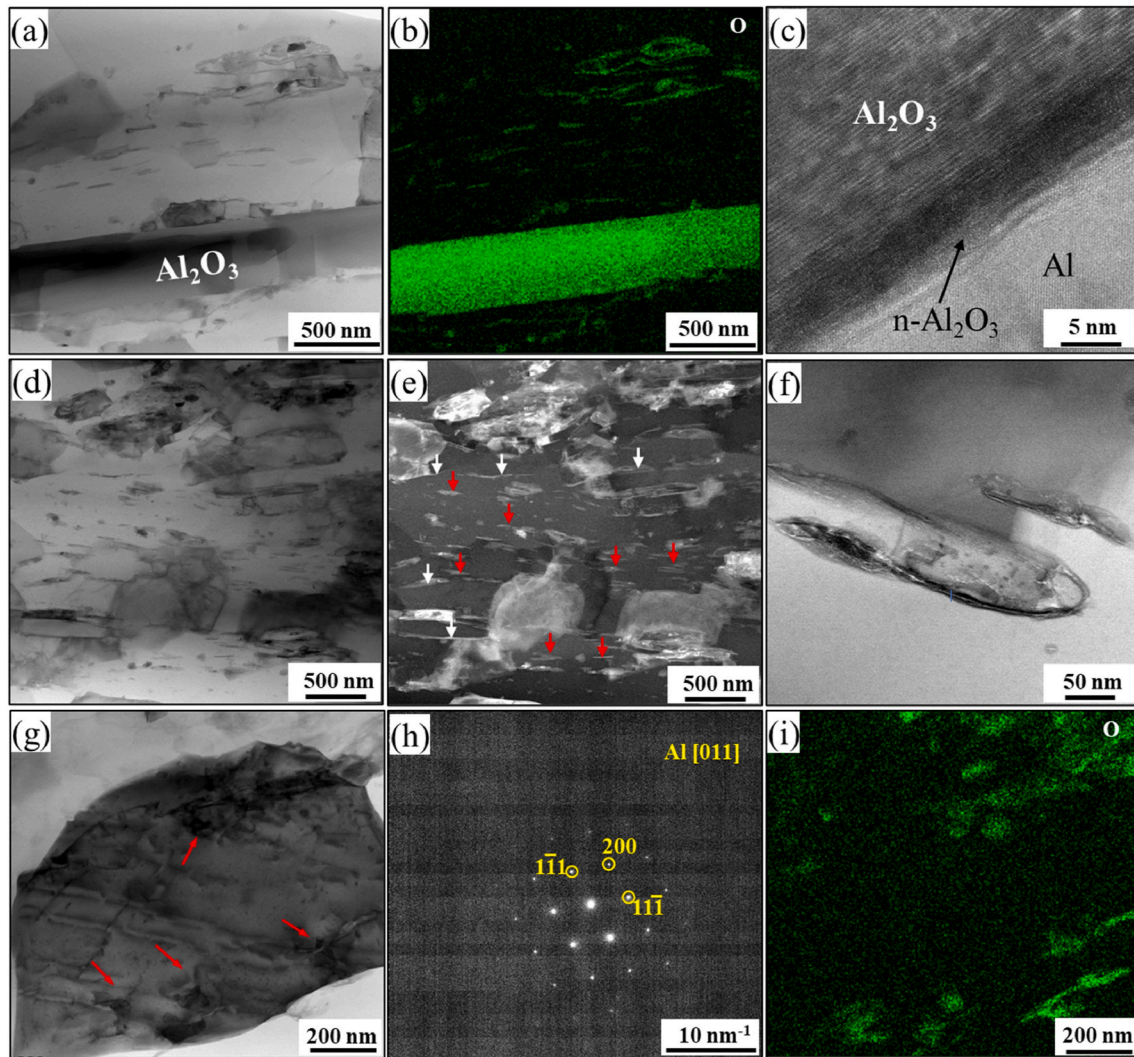

Fig. 4. SEM images of (a) Al$_2$O$_3$/Al, (b) Al$_2$O$_3$-rGO/Al composites.

Fig. 5. (a) BF-STEM images and (b) the corresponding O element mapping of Al$_2$O$_3$/Al composite, (c) HRTEM image at Al$_2$O$_3$/Al interface, (d) BF-STEM and (e) DF-STEM images of Al matrix, (f) BF-STEM image of Al matrix at specific location, showing the bent n-Al$_2$O$_3$, (g) BF-STEM and (h) SEAD pattern, and (i) the correspond O element mapping of Al [011]. White arrows and red arrows respectively indicate intergranular n-Al$_2$O$_3$ and intragranular n-Al$_2$O$_3$. (For interpretation of the references to colour in this figure legend, the reader is referred to the Web version of this article.)

boundary spacing scaled by the interception length along lines perpendicular (d_T) and parallel (d_L) to the extrusion direction is shown in Fig. 7. The grain size of Al matrix ($d_T = 0.86$ μm and $d_L = 2.85$ μm) is higher than that of rGO/Al composites ($d_T = 0.75$ μm and $d_L = 2.7$ μm). The DRX and grain growth could be suppressed due to the pinning effect of intergranular n-Al$_2$O$_3$. During hot-extrusion, the introduction of rGO at GBs could inhibit the broken of n-Al$_2$O$_3$ nanolayers, resulting in more intergranular n-Al$_2$O$_3$. Compared to Al matrix, the grain size is further refined in rGO/Al composites.

3.2. Mechanical properties

Fig. 8(a) shows the tensile stress-strain curves of the composites and Al matrix. The measured data of different samples are listed in Table 1, in which toughness refers to the integration of engineering stress-strain curve. The introduction of individual rGO or Al$_2$O$_3$ into Al matrix can improve the strength and modulus of composites while the total elongation slightly decreases. The ultimate tensile strength of the Al$_2$O$_3$-rGO/Al composite is measured as 270 MPa, higher than the individual reinforced composites. The Al$_2$O$_3$-rGO/Al composite achieves a 60% increase in strength and a notable improvement in toughness (23%) compared to the corresponding Al matrix. The ductility of Al$_2$O$_3$-rGO/Al

composite doesn't decrease while the strength increases compared to Al$_2$O$_3$/Al composites.

According to simple rule of mixture (ROM), the strength of the bio-inspired multiscale laminated composite can be estimated by:

$$\sigma = \sigma_{Al} + \Delta\sigma_{Al_2O_3} + \Delta\sigma_{rGO} \tag{1}$$

where σ_{Al} is the strength of Al matrix, in which the contribution of n-Al$_2$O$_3$ is included. $\Delta\sigma_{Al_2O_3}$ is the stress increment due to the addition of Al$_2$O$_3$, equals to the difference between $\sigma_{Al_2O_3}$ and σ_{Al}, and $\Delta\sigma_{rGO}$ is the stress increment due to the addition of rGO, equals to the difference between σ_{rGO} and σ_{Al}. It is interesting to note that tensile strength in the Al$_2$O$_3$-rGO/Al composite is superior to what is predicted using simple rule of mixture with the contribution of rGO and Al$_2$O$_3$. A shadow region could be drawn between the prediction and experimentally measured curves. As shown in Fig. 8(b), it indicates an extra strengthening, demonstrating a synergetic strengthening in the bioinspired multiscale reinforced composite.

Fig. 8(c) shows the comparison of strain hardening behavior of Al matrix and composites. According to Considere's criterion [25], resistance to necking is determined by strain hardening rate ψ, ψ = dσ/dε, where σ denotes true stress, ε true strain. The strain hardening rate of
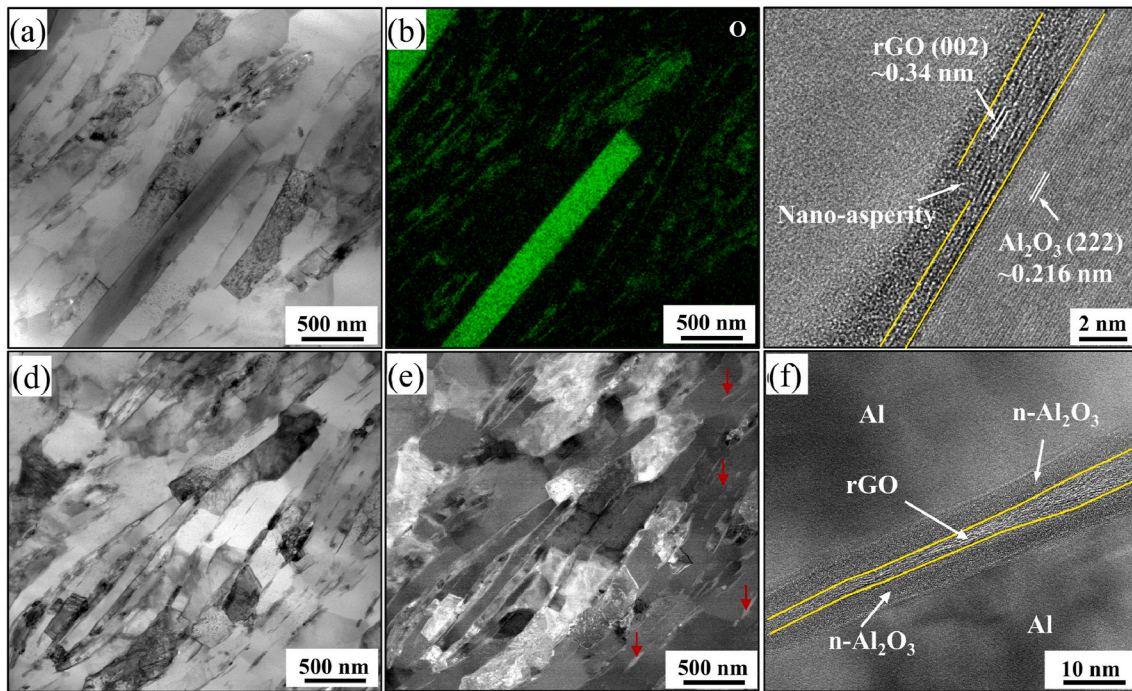
Fig. 6. Bright-field STEM images of (a) Al₂O₃-rGO/Al laminated composite and (b) the corresponding O element mapping, (c) HRTEM image of Al₂O₃/rGO/Al interface, (d, e) Bright-field and Dark-field STEM images of rGO/Al composite. Red arrows indicate intragranular n-Al₂O₃. (e) HRTEM image of Al/rGO/Al interface. (For interpretation of the references to colour in this figure legend, the reader is referred to the Web version of this article.)
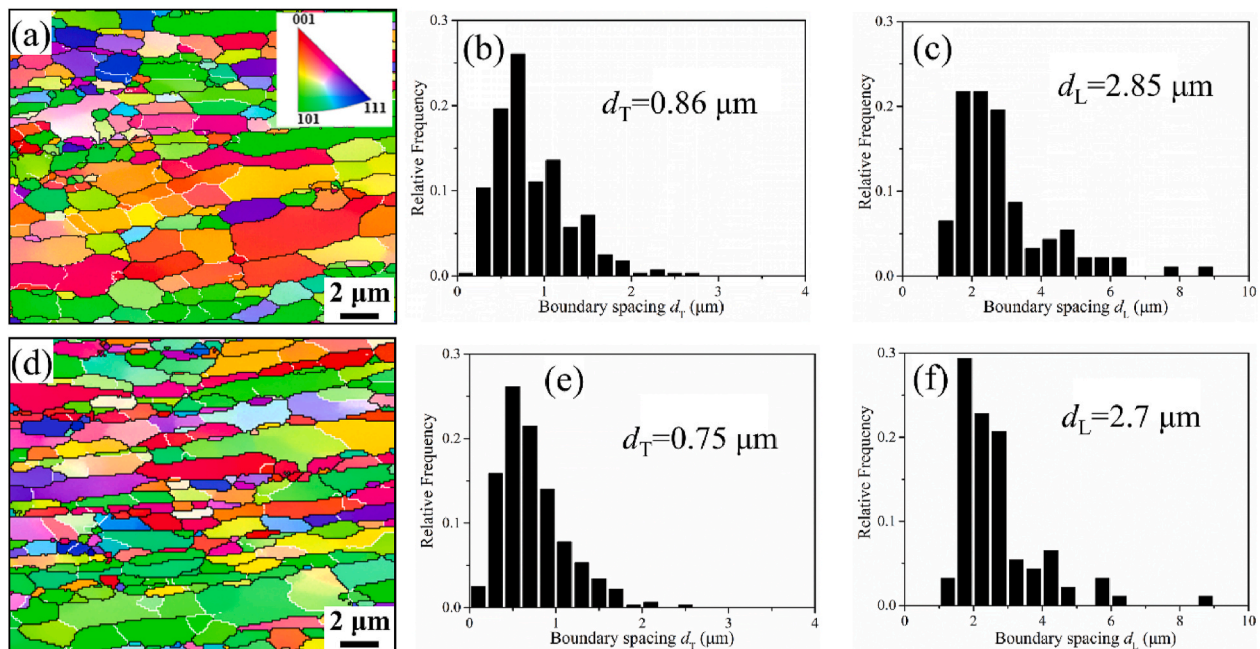

Fig. 7. EBSD images of (a) Al matrix, and (d) rGO/Al composite, the low-angle boundaries ($2° \leq \theta < 15°$) are depicted as white lines, while the high-angle boundaries ($\theta \geq 15°$) are depicted as black lines. The corresponding histograms for boundary spacing distribution of the elongated Al grain along the direction vertical to (b, e) and parallel to (c, f) the extrusion direction in Al matrix and rGO/Al composites.

Al₂O₃-rGO/Al composite is higher that both freestanding rGO/Al and Al₂O₃/Al composites at a low plastic strain stage (0.1%–1.8%). From 1.8% to necking, the strain hardening rate of Al₂O₃-rGO/Al composite is still higher than Al₂O₃/Al composite. Moreover, the strain hardening rate of rGO/Al is higher than that of Al₂O₃/Al. Thus, rGO is a critical factor to obtain graceful strain hardening of Al₂O₃-rGO/Al composite, without sacrificing the uniform elongation compared to Al₂O₃/Al sample.

3.3. Fracture morphology

Fig. 9 shows the fracture morphologies of Al matrix and rGO/Al composite. The Al matrix shows well-developed dimples, indicating a typical ductile fracture with substantial plastic deformation. The
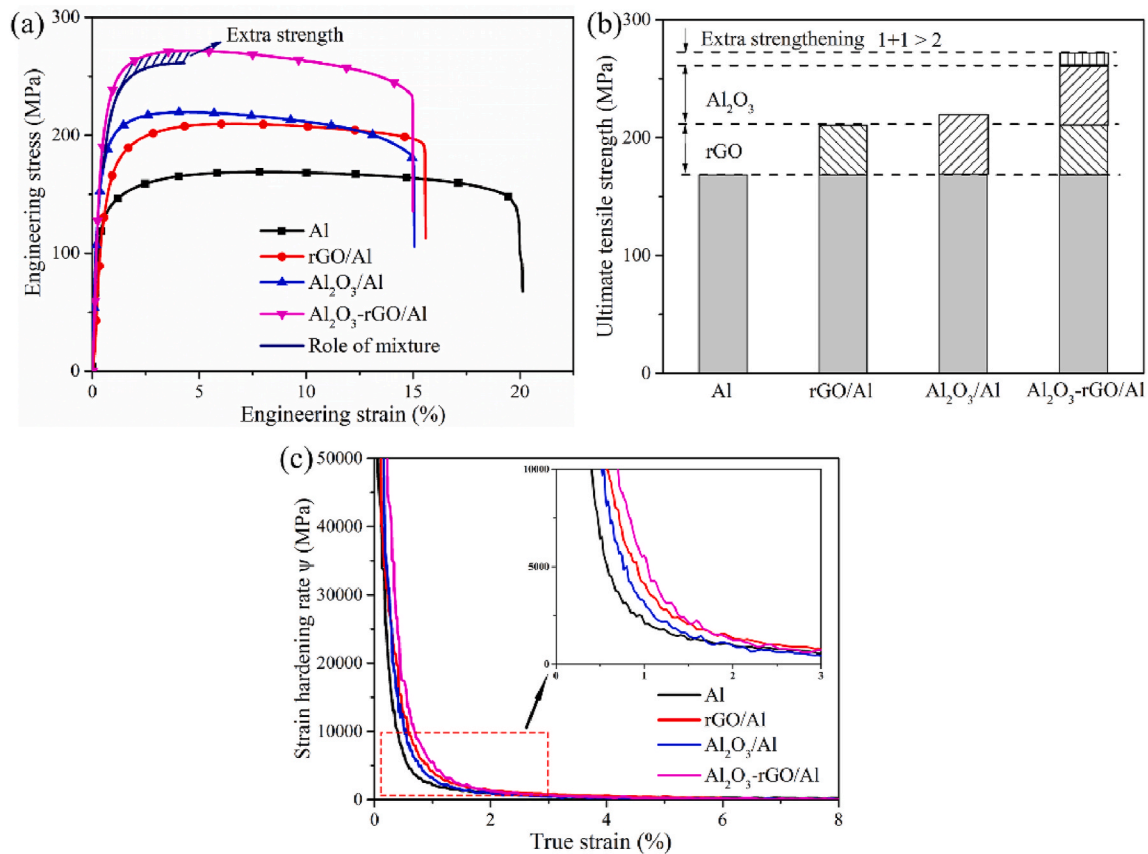
Fig. 8. (a) Tensile properties of Al matrix and composites, (b) Histogram of ultimate tensile strength, (c) Strain hardening curve of Al matrix and composites.

Table 1
Mechanical properties of Al matrix and the composites.

Samples	Elastic modulus/GPa	Yield strength/MPa	Ultimate tensile strength/MPa	Uniform elongation/%	Total elongation/%	Toughness/MJ/m^3
Al	70 ± 0.2	126.5 ± 1.5	168.5 ± 0.5	7.5 ± 0.3	20 ± 0.5	30.5 ± 1
rGO/Al	71.5 ± 0.5	147.8 ± 1	206.5 ± 0.5	6.1 ± 0.1	15.5 ± 0.3	30.7 ± 2
Al_2O_3/Al	81.5 ± 0.5	164 ± 1	219.5 ± 1	4.4 ± 0.2	14.5 ± 0.5	31 ± 1
Al_2O_3-rGO/Al	82.4 ± 0.2	203.5 ± 3	270 ± 2	4.3 ± 0.2	14.7 ± 0.3	37 ± 1

laminated structure is not found in the Al matrix because of grain growth during consolidation at high temperature. With the introduction of rGO, the rGO/Al composite also exhibits ductile failure and the nacre-inspired nanolaminated structure is formed, as shown in Fig. 9(c).

Fig. 10 shows the fracture morphologies of Al_2O_3/Al and Al_2O_3-rGO/Al composites. Both the composites exhibit a common feature of bimodal distribution of dimples, with large dimples near Al_2O_3 and fine dimples, similar to those observed in Al matrix. The phenomenon of pull-out Al_2O_3 is observed in Al_2O_3/Al and Al_2O_3-rGO/Al composites. The difference of both composites is the degree of interfacial debonding. The interfaces between Al_2O_3 and Al are completely separated in the Al_2O_3/Al composite (Fig. 10(b)), but not the whole interfaces are separated in Al_2O_3-rGO/Al composites (Fig. 10 (d)). The introduction of rGO can improve the interface bonding between Al_2O_3 and Al, which delays the pulling out of Al_2O_3.

4. Discussion

4.1. The role of intergranular or intragranular n-Al$_2$O$_3$

In metal matrix composite, for intragranular reinforcement, Orowan mechanism, involving the interaction between the pre-existent dislocations and nanoparticles, plays a major role in strengthening of composite

[26]. When the reinforcements are intergranular, they cannot trap any Orowan loops and load-bearing is the dominant strengthening mechanism. In the study, the intragranular n-Al_2O_3 are observed in Al grain of Al matrix and Al_2O_3/Al composites. The previous studies [27,28] have reported that the formation of intragranular nano-reinforcement is attributed to the occurrence of DRX during hot processing. Once the driving force is larger than the Zener pinning force induced by nano-reinforcement, the grain boundaries would migrate and pass the nano-reinforcements, resulting in the formation of intragranular nano-reinforcement. After the n-Al_2O_3 layer is broken into nano-whiskers with the length of less than 200 nm (Fig. 5(f)), part of them could be left inside the recrystallized Al grains due to DRX. The rGO nanosheets promote n-Al_2O_3 to retain at grain boundaries in rGO/Al or Al_2O_3-rGO/Al laminated composites. A critical question then arises: with respect to intergranular or intragranular n-Al_2O_3, which is better?

Our research group have used the same flake Al and flake Al_2O_3 powders to fabricate the Al matrix and Al_2O_3/Al composite with intergranular n-Al_2O_3 via hot-rolling route [19]. The comparison of mechanical properties is shown in Fig.S1. The uniform elongation and total elongation of the samples with partial intragranular and intergranular n-Al_2O_3 are higher than that of the samples with intergranular n-Al_2O_3, although the yield strength and ultimate tensile strength is slightly
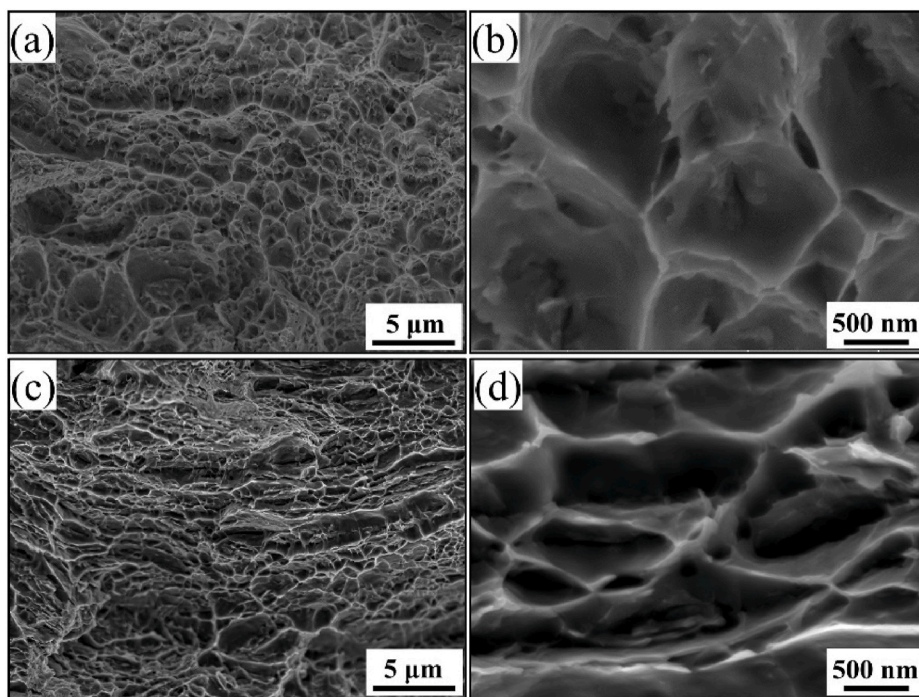
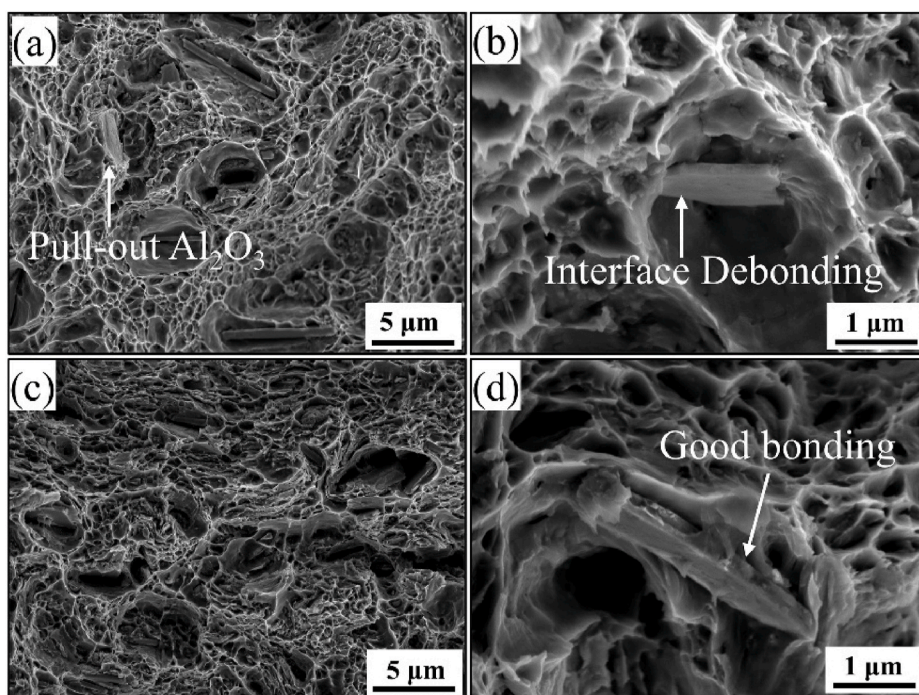**Fig. 9.** Fracture morphology of (a,b) Al matrix and (c,d) rGO/Al composite.

Fig. 10. Fracture morphology of (a,b) Al_2O_3/Al and (c,d) Al_2O_3-rGO/Al composites.

decreased. The locations of n-Al_2O_3 would influence the grain size of Al matrix. Table S1 shows the comparison of grain size and the corresponding strength contribution from Hall-Petch relation in Al matrix with different processing route. The intergranular n-Al_2O_3 can inhibit the grain growth though Zenner pinning, resulting in grain refinement. The difference (3.4 MPa) of strength contribution from Hall-Petch relation is obviously smaller than the difference (29.5 MPa) of yield strength. It is due to load-bearing effect of intergranular n-Al_2O_3 and the higher strain hardening rate (Fig.S1) at the beginning of tensile

deformation. However, as tensile deformation increases, the strain hardening rate dramatically decreases due to the lower dislocation accumulation capacity in smaller Al grain [29]. On the contrary, the intragranular n-Al_2O_3 can store a large number of dislocation loops during tensile deformation, contributing to dislocation accumulation capacity and the uniform elongation. The difference of ultimate tensile strength is only 8.5 MPa, smaller than that of yield strength. Therefore, the phenomenon suggests that the intragranular n-Al_2O_3 has better strengthening and toughening effect, compared with intergranular

n-Al$_2$O$_3$.

In rGO/Al or Al$_2$O$_3$-rGO/Al laminated composites, n-Al$_2$O$_3$ is mainly located at GBs, as shown in Fig. 6. However, their strain hardening rate is higher than the Al matrix and Al$_2$O$_3$/Al composite with partial intragranular n-Al$_2$O$_3$. It suggests that the higher strain hardening is mainly attributed to the introduction of rGO at grain boundaries, rather than the intergranular n-Al$_2$O$_3$. More details will be discussed in the next section.

4.2. Enhanced strain hardening in bioinspired multiscale laminated composite

Strain hardening results from dynamic interaction of dislocations with each other and with various constituents of the microstructure, e.g. forest dislocation, GBs, second phase or reinforcements [30–34]. The strain incompatibility between hard domain (reinforcement) and the soft domain (metal) can produce a high density of geometrically necessary dislocations (GNDs) near the reinforcement/matrix interface, and then a back stress in soft phase is produced to improve the flow stress and work hardening [35]. In Fig. 8(c), the strain hardening rates of all the composites are higher than that of Al matrix. Strain hardening rate of rGO/Al is higher than that of Al$_2$O$_3$/Al composite after true strain of 0.3%, while the volume fraction of Al$_2$O$_3$ is thirty times than that of rGO. Interface effect is a key mechanism for the deformation of metal matrix composites reinforced with nanoreinforcements. Jiang et al. [33] found that the higher strain hardening rate of graphene nanosheets (GNS) reinforced Al composite is determined by GNS/Al interface, which mainly promotes forest hardening by producing additional interface-stored dislocations and strain gradient GNDs. Li et al. [36] found that the introduction of rGO into Cu matrix could reduce the grain-boundary energy, enabling concurrent dislocation storage near the boundaries. Kim et al. [37] found that the two-dimensional geometry, high intrinsic strength and modulus of graphene can effectively constrain dislocation motion and propagation across metal-graphene interface.

To probe the origins of higher stain hardening rates of rGO/Al and Al$_2$O$_3$-rGO/Al laminated composites than Al$_2$O$_3$/Al composite, tensile

loading-unloading test at intervals of 0.5% nominal strain were performed to investigate the Bauschinger effect, as shown in Fig. 11, thereby estimating the effective and back stresses. The method has been widely discussed in previous study [33,34,38,39]. Back stress belongs to long-range internal stress produced by GNDs, which will be blocked by and pile up against domain boundaries [35]. As shown in Fig. 11(a), the Al$_2$O$_3$-rGO/Al laminated composite shows larger hysteresis loop, that is stronger Bauschinger effect than the individual rGO/Al and Al$_2$O$_3$/Al composites. Fig. 11(b) exhibits the method referred to Yang et al. [38] to calculate back stress (σ_b) using a single unloading-reloading loop, as follows:

$$\sigma_b = \frac{\sigma_u + \sigma_r}{2} \tag{2}$$

where σ_u is the unloading yield stress and σ_r is the reloading yield stress. Each yield point is defined as the point which has a 10% reduction in slop from the effective elastic modulus.

As shown in Fig. 11(c–e), both back stress and effective stress increase with the addition of rGO or Al$_2$O$_3$ in Al, resulting in the strengthening of composites. The back stress and effective stress of rGO-Al$_2$O$_3$/Al composite is higher than the individual reinforced composites. The back stress of rGO/Al composite is higher than that of Al$_2$O$_3$/Al composite after the true strain of 2.5%, although the lower back stress before the true strain of 2.5%. To explore the interesting phenomenon, the derivation of back stress needs to be clarified. Back stress has two origins [32,40], i.e., intragranular one that arises from the heterogeneous dislocation distribution such as dislocation cells and walls, and the intergranular one that results from plastic strain incompatibilities between hard and soft domains, such as bimodal grains, or the interface between reinforcement and matrix. Here, we only consider the comparison of intergranular back stress that is produced by reinforcement, i. e., rGO and Al$_2$O$_3$ in the study. Xu et al. [29] discussed that the back stress at the macroscale contains the load transfer to the reinforcements during the plastic stage. The strengthening from load transfer consists of the load transferred to reinforcement at elastic limit ($\Delta\sigma_{L-T}$) and the increase of back stress induced by the reinforcement/matrix interface with the true stain ($\Delta\sigma_{Back-R}$). The $\Delta\sigma_{L-T}$ of Al$_2$O$_3$/Al (15.5 MPa) is
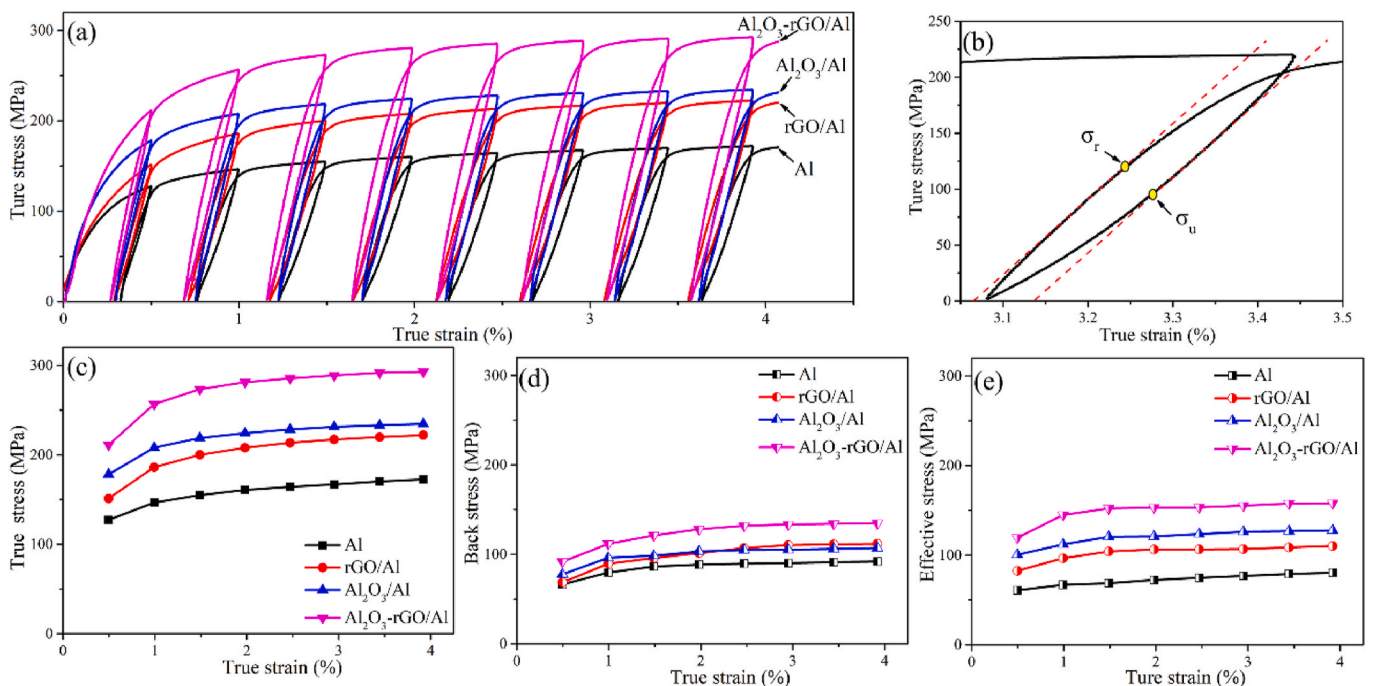

Fig. 11. (a) LUR stress-strain curves, (b) the measured hysteresis loop with σ_u and σ_r defined at the true strain of 3.44%, (c) the flow stress, (d) back stress and (e) effective stress of Al, rGO/Al, Al$_2$O$_3$/Al and Al$_2$O$_3$-rGO/Al.

obviously higher than that of rGO/Al (4.5 MPa). The theoretical calculation of $\Delta\sigma_{L-T}$ is shown in next section. At the beginning of tensile deformation (~0.5%), the higher back stress in Al$_2$O$_3$/Al composite results from higher $\Delta\sigma_{L-T}$. As the true strain increases, the increasing rate of back stress in rGO/Al composite is higher than that in Al$_2$O$_3$/Al composite, while the increasing rate of effective stress is nearly the same. It indicates that more dislocations are constrained near rGO/Al interface, producing a higher long-range internal stress and thus improving the $\Delta\sigma_{Back-R}$. The increased back stress is responsible for higher strain hardening in rGO/Al than Al$_2$O$_3$/Al composites after true strain of 0.5%. Similar increase of back stress induced strain hardening was also reported in CNT/Al [34]. Therefore, in the bioinspired multiscale Al$_2$O$_3$-rGO/Al laminated composite, the higher strain hardening capacity is the synergistic effect of Al$_2$O$_3$ and rGO, in which the load-transfer of Al$_2$O$_3$ mainly provide the strain hardening rate at the beginning of tensile deformation (0.5%) and the back stress induced strain hardening due to the rGO/Al interface after the true strain of 0.5%.

4.3. Extra-strengthening mechanism in bioinspired multiscale laminated composite

Tensile strength of the bioinspired multiscale Al$_2$O$_3$-rGO/Al laminated composite exhibits extra-strengthening mechanism, as shown in Fig. 8, compared with what is predicted using simple rule of mixture with the contribution of rGO and Al$_2$O$_3$. The strengthening mechanism for bioinspired multiscale laminated composite is not a simply superposition of the strengthening effects produced by individual reinforcement, but the synergistic effect of each reinforcing mechanism. The strengthening mechanisms of MMCs could be categorized to four types [41]: Hall-Petch strengthening by grain refinement, load transfer strengthening, coefficient of thermal expansion (CTE) mismatch strengthening, and Orowan looping strengthening. The load transfer and CTE mismatch strengthening are mainly strengthening mechanism due to the addition of Al$_2$O$_3$. The yield strength of the Al$_2$O$_3$/Al and Al$_2$O$_3$-rGO/Al composites in the study can be expressed as:

$$\sigma_{Al_2O_3/Al} = \sigma_{Al} + \Delta\sigma_{CTE}^{Al_2O_3} + \Delta\sigma_{L-T}^{Al_2O_3} \tag{3}$$

$$\sigma_{Al_2O_3-rGO/Al} = \sigma'_{Al} + \Delta\sigma_{H-P} + \Delta\sigma_{CTE}^{rGO} + \Delta\sigma_{L-T}^{rGO} + \Delta\sigma_{CTE}^{Al_2O_3} + \Delta\sigma_{L-T}^{Al_2O_3}$$
$$= \sigma_{rGO/Al} + \Delta\sigma_{CTE}^{Al_2O_3} + \Delta\sigma_{L-T}^{Al_2O_3} \tag{4}$$

where σ_{Al} is the yield strength of Al matrix, containing the intergranular and intragranular n-Al$_2$O$_3$. σ'_{Al} is the yield strength of Al matrix, only containing intergranular n-Al$_2$O$_3$. $\Delta\sigma_{CTE}^{Al_2O_3}$ and $\Delta\sigma_{CTE}^{rGO}$ are the CTE strengthening term of rGO and Al$_2$O$_3$. $\Delta\sigma_{L-T}^{rGO}$ and $\Delta\sigma_{L-T}^{Al_2O_3}$ are the load strengthening term of rGO and Al$_2$O$_3$. $\Delta\sigma_{H-P}$ is the strengthening effect of grain refinement.

The improvements to yield strength due to CTE strengthening can be expressed as [41]:

$$\Delta\sigma_{CTE} = 1.25Gb\left(\frac{V_r}{1-V_r}\frac{12\Delta CTE \times \Delta T}{b}\right)^{1/2}\left(\frac{1}{\bar{d}}\right)^{1/2} \tag{5}$$

where G is the shear modulus of the matrix (25.4 GPa), b is the burgers vector of matrix (0.286 nm), V_r is the volume fraction of Al$_2$O$_3$ (0.05), ΔCTE is the difference between the matrix and the reinforcement (15.9 × 10^{-6} K^{-1}), ΔT is the difference in temperature between the hot processing and room temperature (400 K). $\bar{d}$ is the equivalent diameter of Al$_2$O$_3$ (2.3 μm). According to equation (4), the increment (22 MPa) of $\Delta\sigma_{CTE}^{Al_2O_3}$ is same in Al$_2$O$_3$/Al and Al$_2$O$_3$-rGO/Al composites. Fig. 12(a) shows the comparison of the increment to yield strength due to different strengthening mechanism from Al$_2$O$_3$. It is observed that the load transfer of Al$_2$O$_3$ (34 MPa) in Al$_2$O$_3$-rGO/Al composite is higher than that (15.5 MPa) in Al$_2$O$_3$/Al composite. According to the shear-lag model, the applied stress is transferred to the Al$_2$O$_3$ platelets through the interfacial shear stress τ developed in the Al matrix [17]. The phenomenon of pull-out Al$_2$O$_3$ is observed in Fig. 10, suggesting that the interfacial shear stress τ is smaller than a critical interfacial stress τ$_c$. As shown in Fig. 12(b), the force balance between the interfacial shear stress and the reinforcement tensile stress for the case of composites containing flake Al$_2$O$_3$ is expressed as follows [42]:

$$\tau\left(\frac{S}{l}\right)dx = Ad\sigma_p \tag{6}$$

where S and A are respectively the interfacial area ($2l^2+2lh$) and cross-section (lh) of Al$_2$O$_3$. l, h are the length (~4 μm) and thickness (~0.4 μm) of Al$_2$O$_3$ from statistically estimation from SEM images. x is the distance from the edge of Al$_2$O$_3$, and σ_p is the (position specific) tensile stress of Al$_2$O$_3$. When the maximum stress reaches the tensile strength of the reinforcement, the reinforcement length is a critical length (l_c) and the critical interfacial stress τ$_c$ of the reinforcement, which is expressed as:

$$l_c = \frac{\sigma_r h}{2\tau_m} - h \tag{7}$$

$$\tau_c = \frac{\sigma_r h}{2(l+h)} \tag{8}$$

where σ_r is the tensile strength of Al$_2$O$_3$ (2 GPa) [17]. τ_m is the shear stress of matrix (equal to $\sigma_m/\sqrt{3}$). From the above microstructural and mechanical analysis, the location of n-Al$_2$O$_3$ can influence the mechanical properties. The yield strength of rGO/Al is considered as the strength of matrix in Al$_2$O$_3$-rGO/Al composite. l_c values calculated for Al$_2$O$_3$ are ~5.1, 4.4 μm respectively in Al$_2$O$_3$/Al and Al$_2$O$_3$-rGO/Al composites, which are larger than the length of Al$_2$O$_3$. τ$_c$ is calculated for Al$_2$O$_3$ is ~87 MPa. Based on the shear-lag model under the pull-out model [42], the load-transfer strengthening effect ($\Delta\sigma_{L-T}$) can be estimated by:
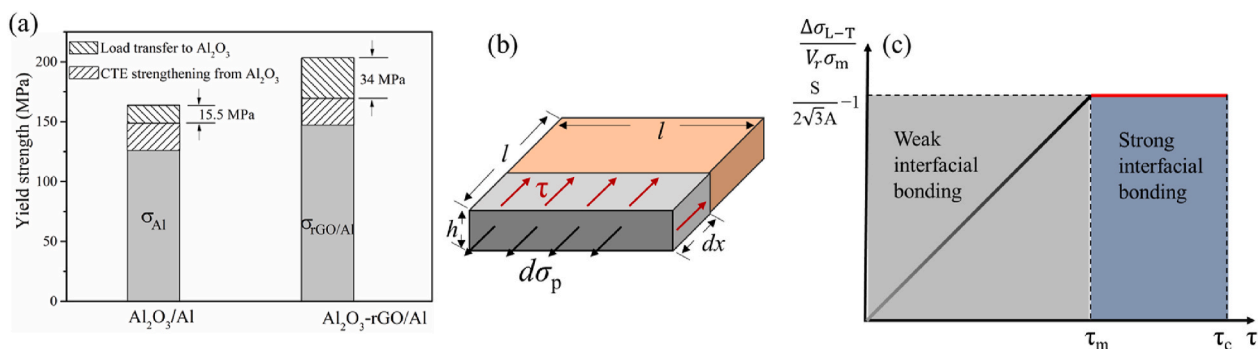

Fig. 12. (a) Strength contribution of load transfer and CTE strengthening from Al$_2$O$_3$ in Al$_2$O$_3$ and Al$_2$O$_3$-rGO/Al composites, (b) Depiction of the balance between tensile stress and shear stress of individual Al$_2$O$_3$, (c) The relation between load transfer strengthening efficiency and interfacial shear stress.

$$\Delta\sigma_{L-T} = V_r\left(\frac{S}{A}\right)\left(\frac{\tau}{2}\right) - \sigma_m V_r; \; for \; \tau < \tau_m \qquad (9)$$

$$\Delta\sigma_{L-T} = V_r\left(\frac{S}{A}\right)\left(\frac{\tau_m}{2}\right) - \sigma_m V_r; \; for \; \tau_m \leq \tau \leq \tau_c \qquad (10)$$

In Al$_2$O$_3$/Al composite, the theoretical value of $\Delta\sigma_{L-T}$ (40 MPa), which is calculated by equation (10), is overestimated and higher than experimental value (15.5 MPa). As shown in Fig. 12(c), when the interfacial shear stress is smaller than the shear stress of matrix, the load transfer strengthening efficiency would decrease as the interfacial shear stress decrease. The calculated interfacial shear stress (75 MPa) in Al$_2$O$_3$-rGO/Al composite is higher than that (37 MPa) in Al$_2$O$_3$/Al composite. Increasing interfacial shear stress is of great importance in composites because it can improve the load-transfer efficiency between reinforcement and matrix. The interfacial bonding strength is closely related to interface structure. The previous studies [43,44] found that n-Al$_2$O$_3$ layer between Al matrix and reinforcement would weaken the strengthening effect of reinforcement. If rGO nanosheets with the same thickness are added between the Al$_2$O$_3$–Al/interface, the strengthening effect of Al$_2$O$_3$ could not be significantly improved due to the existence of n-Al$_2$O$_3$ layer. Once the composite is loaded along the aligned Al$_2$O$_3$, nano-asperity at Al$_2$O$_3$-rGO-Al interface would contribute to the mechanical interlocking, resulting in the improvement of load transfer capacity. Interface bonding is enhanced by nano-asperity at the Al$_2$O$_3$-rGO-Al interface. From the facture morphology in Fig. 10, the introduction of rGO contributes to good interface bonding between Al$_2$O$_3$ and Al. Therefore, the extra-strengthening mechanism could be attributed to enhanced load-transfer due to good bonding at Al$_2$O$_3$/r-GO/Al interface.

4.4. Relationship among modulus-strength-ductility

Both Young's modulus and strength are critical parameters for designing lightweight structure. The introduction of reinforcement is only an effective method to improve the Young's modulus of Al matrix composites, except for Al–Li based alloy [45]. Higher volume fraction of reinforcements can result in higher modulus and strength of composites, but the ductility dramatically decreases due to the quick hardening saturation [46]. On the contrary, the increase of strength is not dependent on the volume fraction reinforcement. The effect of reinforcement size on strength of composite is non-negligible. Tjong [47] reviewed that the strength and ductility of composites could be enhanced by decreasing reinforcement size from micrometer to nanometer level. The nanofillers could allow for the dissipation of strain/stress during deformation in metal matrix nanocomposites (MMNCs), which exhibited an enhanced plasticity relative to the same material reinforced with micro-particles [48]. Unfortunately, the enhancement of Youngs' modulus of MMNCs is restricted due to low volume fraction of nano-reinforcements. Fig. 13 shows the radar chart of final properties of rGO/Al, Al$_2$O$_3$/Al, and Al$_2$O$_3$-rGO/Al. It is observed that the bioinspired multiscale Al$_2$O$_3$-rGO/Al laminated composite exhibits excellent mechanical properties. It can take advantage of higher modulus for microscale Al$_2$O$_3$/Al composite and higher strain hardening rate for rGO/Al composite. The synergistic strengthening effect of multiscale Al$_2$O$_3$-rGO reinforcements can further improve the strength of single-scale reinforced composites. Therefore, the bioinspired multiscale laminated strategy is a desirable method to design and fabricate high-performance engineering materials with simultaneous enhancement of the modulus-strength-ductility.

5. Conclusion

In conclusion, inspired by nacre's multiscale reinforcing mechanism, bioinspired multiscale Al$_2$O$_3$-rGO/Al laminated composite is fabricated by flake powder metallurgy. A systematic study has been conducted to investigate the microstructures and properties correlation of composites.
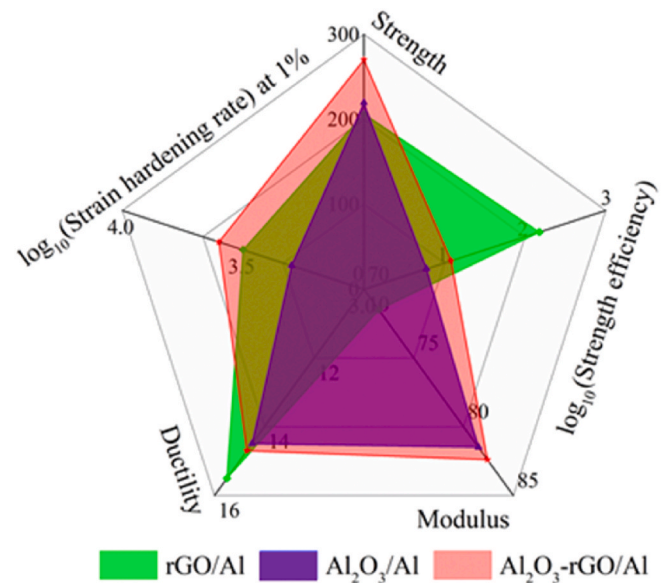

Fig. 13. Radar chart of final properties of rGO/Al, Al$_2$O$_3$/Al, and Al$_2$O$_3$-rGO/Al.

The main conclusions can be summarized in the following:

1) The n-Al$_2$O$_3$ layers at grain boundaries were broken and many of them were left inside the recrystallized Al grains due to DRX, resulting in the formation of intragranular n-Al$_2$O$_3$ with the length of about 200 nm. It is found that the intragranular n-Al$_2$O$_3$ has better strengthening and toughening effect, compared with intergranular n-Al$_2$O$_3$.

2) The introduction of rGO at GBs could inhibit the broken of n-Al$_2$O$_3$ nanolayers and the dynamic recrystallization was further suppressed. The addition of hierarchically aligned Al$_2$O$_3$ and rGO into the Al matrix constitute the nacre-inspired multiscale Al$_2$O$_3$-rGO/Al laminated composite with brick-and-mortar structure.

3) The tensile strength in the Al$_2$O$_3$-rGO/Al laminated composite is superior to what is predicted using simple rule of mixture with the contribution of rGO and Al$_2$O$_3$. The extra-strengthening mechanism is attributed to enhanced load-transfer due to good bonding at Al$_2$O$_3$/rGO/Al interface.

4) In Al$_2$O$_3$-rGO/Al laminated composite, the higher strain hardening capacity is the synergistic effect of Al$_2$O$_3$ and rGO, in which the load-transfer of Al$_2$O$_3$ mainly provide the strain hardening rate at the beginning of tensile deformation (0.5%) and the back stress induced strain hardening due to the rGO/Al interface after the true strain of 0.5%.

5) Balance between modulus-strength-ductility in bioinspired multiscale laminated composite is improved compared to the composite using only individual reinforcement. The present bioinspired multiscale laminated concept can be extended to others' combination of micro-reinforcements and nanofillers for developing advanced composites with simultaneous enhancement of the modulus-strength-ductility.

Credit authorship contribution statement

Zhiming Zhang: Conceptualization, Investigation, Data curation, Writing – original draft, Writing – review & editing. Genlian Fan: Investigation, Methodology, Writing – review & editing. Zhanqiu Tan: Investigation. Haitao Zhao: Investigation. Yanjin Xu: Methodology. Ding-Bang Xiong: Supervision. Zhiqiang Li: Supervision, Project administration, Writing – review & editing, Funding acquisition.

Declaration of competing interest

The authors declare that they have no known competing financial interests or personal relationships that could have appeared to influence the work reported in this paper.

Acknowledgements

Appendix A. Supplementary data

Supplementary data to this article can be found online at https://doi.org/10.1016/j.compositesb.2021.108916.

References

[1] Zhao H, Yang Z, Guo L. Nacre-inspired composites with different macroscopic dimensions: strategies for improved mechanical performance and applications. NPG Asia Mater 2018;10(4):1–22.

[2] Sun J, Bhushan B. Hierarchical structure and mechanical properties of nacre: a review. RSC Adv 2012;2(20):7617–32.

[3] Studart AR. Towards high-performance bioinspired composites. Adv Mater 2012; 24(37):5024–44.

[4] Espinosa HD, Juster AL, Latourte FJ, Loh OY, Gregoire D, Zavattieri PD. Tablet-level origin of toughening in abalone shells and translation to synthetic composite materials. Nat Commun 2011;2(1):173.

[5] Song N, Zhang Y, Gao Z, Li X. Bioinspired, multiscale reinforced composites with exceptionally high strength and toughness. Nano Lett 2018;18(9):5812–20.

[6] Ji B, Gao H. Mechanical properties of nanostructure of biological materials. J Mech Phys Solid 2004;52(9):1963–90.

[7] Wang J, Qiao J, Wang J, Zhu Y, Jiang L. Bioinspired hierarchical alumina–graphene oxide–poly(vinyl alcohol) artificial nacre with optimized strength and toughness. ACS Appl Mater Interfaces 2015;7(17):9281–6.

[8] Launey ME, Munch E, Alsem DH, Barth HB, Saiz E, Tomsia AP, et al. Designing highly toughened hybrid composites through nature-inspired hierarchical complexity. Acta Mater 2009;57(10):2919–32.

[9] Bouville F, Maire E, Meille S, Van de Moortèle B, Stevenson AJ, Deville S. Strong, tough and stiff bioinspired ceramics from brittle constituents. Nat Mater 2014;13: 508.

[10] Li S, Su Y, Jin H, Huang Y, Ouyang Q, Zhang D. Effects of carbon nanotube content on morphology of SiCp(CNT) hybrid reinforcement and tensile mechanical properties of SiCp(CNT)/Al composites. J Mater Res 2017;32(7):1239–47.

[11] Li S, Su Y, Ouyang Q, Zhang D. In-situ carbon nanotube-covered silicon carbide particle reinforced aluminum matrix composites fabricated by powder metallurgy. Mater Lett 2016;167:118–21.

[12] Li S, Su Y, Zhu X, Jin H, Ouyang Q, Zhang D. Enhanced mechanical behavior and fabrication of silicon carbide particles covered by in-situ carbon nanotube reinforced 6061 aluminum matrix composites. Mater Des 2016;107:130–8.

[13] Zhou MY, Ren LB, Fan LL, Tun KS, Gupta M, Zhang YWX, et al. Achieving ultra-high strength and good ductility in AZ61 alloy composites containing hybrid micron SiC and carbon nanotubes reinforcements. Mat Sci Eng A-Struct 2019;768: 138447.

[14] Zhang Y, Gong S, Zhang Q, Ming P, Wan S, Peng J, et al. Graphene-based artificial nacre nanocomposites. Chem Soc Rev 2016;45(9):2378–95.

[15] Li Z, Guo Q, Li Z, Fan G, Xiong D-B, Su Y, et al. Enhanced mechanical properties of graphene (reduced graphene oxide)/aluminum composites with a bioinspired nanolaminated structure. Nano Lett 2015;15(12):8077–83.

[16] Cao M, Xiong D-B, Tan Z, Ji G, Amin-Ahmadi B, Guo Q, et al. Aligning graphene in bulk copper: nacre-inspired nanolaminated architecture coupled with in-situ processing for enhanced mechanical properties and high electrical conductivity. Carbon 2017;117:65–74.

[17] Bonderer LJ, Studart AR, Gauckler LJ. Bioinspired design and assembly of platelet reinforced polymer films. Science 2008;319(5866):1069.

[18] Erb RM, Libanori R, Rothfuchs N, Studart AR. Composites reinforced in three dimensions by using low magnetic fields. Science 2012;335(6065):199.

[19] Zhang Z, Li Z, Tan Z, Zhao H, Fan G, Xu Y, et al. Bioinspired hierarchical Al2O3/Al laminated composite fabricated by flake powder metallurgy. Composites Part A-Appl S 2021;140:106187.

[20] Li Z, Fan G, Tan Z, Guo Q, Xiong D, Su Y, et al. Uniform dispersion of graphene oxide in aluminum powder by direct electrostatic adsorption for fabrication of graphene/aluminum composites. Nanotechnology 2014;25(32).

[21] Li Z, Fan G, Tan Z, Li Z, Guo Q, Xiong D, et al. A versatile method for uniform dispersion of nanocarbons in metal matrix based on electrostatic interactions. Nano-Micro Lett 2016;8(1):54–60.

[22] Asgharzadeh H, Sedigh M. Synthesis and mechanical properties of Al matrix composites reinforced with few-layer graphene and graphene oxide. J Alloys Compd 2017;728:47–62.

[23] Wang Q, Ramírez C, Watts CS, Borrero-López O, Ortiz AL, Sheldon BW, et al. Fracture, fatigue, and sliding-wear behavior of nanocomposites of alumina and reduced graphene-oxide. Acta Mater 2020;186:29–39.

[24] Han Y, Ke Y, Shi Y, Liu Y, Yang G, Li Z, et al. Improved mechanical property of nanolaminated graphene (reduced graphene oxide)/Al–Mg–Si composite rendered by facilitated ageing process. Mat Sci Eng A-Struct 2020;787:139541.

[25] Hart EW. A theory for flow of polycrystals. Acta Metall 1967;15(9):1545–9.

[26] Zhang Z, Chen DL. Contribution of Orowan strengthening effect in particulate-reinforced metal matrix nanocomposites. Mat Sci Eng A-Struct 2008;483–484: 148–52.

[27] Li AB, Wang GS, Zhang XX, Li YQ, Gao X, Sun H, et al. Enhanced combination of strength and ductility in ultrafine-grained aluminum composites reinforced with high content intragranular nanoparticles. Mat Sci Eng A-Struct 2019;745:10–9.

[28] Zan YN, Zhou YT, Zhao H, Liu ZY, Wang QZ, Wang D, et al. Enhancing high-temperature strength of (B4C+Al2O3)/Al designed for neutron absorbing materials by constructing lamellar structure. Compos B Eng 2020;183:107674.

[29] Xu R, Tan Z, Fan G, Ji G, Li Z, Guo Q, et al. Microstructure-based modeling on structure-mechanical property relationships in carbon nanotube/aluminum composites. Int J Plast 2019;120:278–95.

[30] Fribourg G, Bréchet Y, Deschamps A, Simar A. Microstructure-based modelling of isotropic and kinematic strain hardening in a precipitation-hardened aluminium alloy. Acta Mater 2011;59(9):3621–35.

[31] Delincé M, Bréchet Y, Embury JD, Geers MGD, Jacques PJ, Pardoen T. Structure–property optimization of ultrafine-grained dual-phase steels using a microstructure-based strain hardening model. Acta Mater 2007;55(7):2337–50.

[32] Feaugas X. On the origin of the tensile flow stress in the stainless steel AISI 316L at 300 K: back stress and effective stress. Acta Mater 1999;47(13):3617–32.

[33] Jiang Y, Xu R, Tan Z, Ji G, Fan G, Li Z, et al. Interface-induced strain hardening of graphene nanosheet/aluminum composites. Carbon 2019;146:17–27.

[34] Xu R, Fan G, Tan Z, Ji G, Chen C, Beausir BT, et al. Back stress in strain hardening of carbon nanotube/aluminum composites. Mater Res Lett 2017;6(2):113–20.

[35] Zhu Y, Wu X. Perspective on hetero-deformation induced (HDI) hardening and back stress. Mater Res Lett 2019;7(10):393–8.

[36] Li Z, Wang H, Guo Q, Li Z, Xiong D-B, Su Y, et al. Regain strain-hardening in high-strength metals by nanofiller incorporation at grain boundaries. Nano Lett 2018;18 (10):6255–64.

[37] Kim Y, Lee J, Yeom MS, Shin JW, Kim H, Cui Y, et al. Strengthening effect of single-atomic-layer graphene in metal–graphene nanolayered composites. Nat Commun 2013;4(1):2114.

[38] Yang M, Pan Y, Yuan F, Zhu Y, Wu X. Back stress strengthening and strain hardening in gradient structure. Mater Res Lett 2016;4(3):145–51.

[39] Wu X, Yang M, Yuan F, Wu G, Wei Y, Huang X, et al. Heterogeneous lamella structure unites ultrafine-grain strength with coarse-grain ductility. P Natl Acad Sci USA 2015;112(47):14501.

[40] Li J, Lu W, Chen S, Liu C. Revealing extra strengthening and strain hardening in heterogeneous two-phase nanostructures. Int J Plast 2020;126:102626.

[41] Zhou MY, Ren LB, Fan LL, Zhang YWX, Lu TH, Quan GF, et al. Progress in research on hybrid metal matrix composites. J Alloys Compd 2020;838:155274.

[42] Shin SE, Choi HJ, Shin JH, Bae DH. Strengthening behavior of few-layered graphene/aluminum composites. Carbon 2015;82:143–51.

[43] Fan G, Jiang Y, Tan Z, Guo Q, Xiong D-b, Su Y, et al. Enhanced interfacial bonding and mechanical properties in CNT/Al composites fabricated by flake powder metallurgy. Carbon 2018;130:333–9.

[44] Liu ZY, Wang LH, Zan YN, Wang WG, Xiao BL, Wang D, et al. Enhancing strengthening efficiency of graphene nano-sheets in aluminum matrix composite by improving interface bonding. Compos B Eng 2020;199:108268.

[45] Noble B, Harris SJ, Dinsdale K. The elastic modulus of aluminium-lithium alloys. J Mater Sci 1982;17(2):461–8.

[46] Kim C-S, Cho K, Manjili MH, Nezafati M. Mechanical performance of particulate-reinforced Al metal-matrix composites (MMCs) and Al metal-matrix nano-composites (MMNCs). J Mater Sci 2017;52(23):13319–49.

[47] Tjong SC. Novel nanoparticle-reinforced metal matrix composites with enhanced mechanical properties. Adv Eng Mater 2007;9(8):639–52.

[48] Jiang L, Ma K, Yang H, Li M, Lavernia EJ, Schoenung JM. The microstructural design of trimodal aluminum composites. JOM (J Occup Med) 2014;66(6): 898–908.